Ocean Engineering 232 (2021) 109130

Contents lists available at ScienceDirect

Ocean Engineering

journal homepage: www.elsevier.com/locate/oceaneng

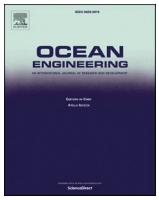

Experimental and numerically obtained low-frequency radiation characteristics of the OC5-DeepCwind semisubmersible

Haoran Li [a,*], Erin E. Bachynski-Polić [a,b]

[a] Department of Marine Technology, Norwegian University of Science and Technology (NTNU), Trondheim, Norway
[b] Centre for Autonomous Marine Operations and Systems (AMOS), NTNU, Trondheim, Norway

ARTICLE INFO

Keywords:
Semi-submersible floating wind turbine
CFD
OpenFOAM
Potential flow theory
Added mass
Hydrodynamic damping

ABSTRACT

Added mass and damping play a significant role in accurate prediction of floating wind turbine (FWT) motions, especially near the resonance frequencies. This paper investigates the still-water hydrodynamic characteristics of a semi-submersible FWT around the natural periods of surge, heave and pitch motion. A higher-fidelity tool (Computational Fluid Dynamics, CFD) based on OpenFOAM is employed in the numerical computations. The tool is validated against experimental measurements (decay tests and forced surge motions) and then applied to investigate the hydrodynamic characteristics of the whole floater and each column at different amplitudes of forced motions. The heave and pitch decay match well with the experimental measurements, whereas the CFD simulations underestimate the damping in the surge decay. However, better agreement is obtained between measured and numerically estimated surge force in the forced oscillations in surge. Furthermore, the added mass derived from the CFD simulation is around 12% larger than that estimated by the potential flow theory, except the estimated heave added mass under the largest heave motion (up to 35% larger). This additional added mass in the CFD simulations is due to the viscous effects. The damping shows a small dependence on the oscillation period and a larger dependence on the oscillation amplitude within the tested period range. At these frequencies, radiation damping is completely negligible compared to the viscous damping due to vortex shedding, and the accuracy of Morison's drag forces in capturing the viscous damping is sensitive to the drag coefficient.

1. Introduction

As a promising way of harnessing the energy from winds over deep water and farther offshore, floating wind turbines (FWTs) have gained more and more attentions in recent years, especially semi-submersible FWTs (Peiffer et al., 2011). One type of semi-submersible FWTs consists of four cylindrical columns linked with a set of braces (Robertson et al., 2014, 2016). In order to reduce the amplitude of the heave resonance and move the heave resonance periods outside the wave frequency range, heave plates are attached to the base of some columns. These plates provide additional added mass and enhance the flow separation and vortex shedding processes that provide viscous damping (WEI et al., 2010). All these factors reduce the floater motions, but also generate more stringent requirements for the fidelity of simulation tools. Most approaches use potential flow theory and Morison's equation to evaluate the hydrodynamic forces on the floater (Cordle and Jonkman, 2011). However, in Phase II of the OC5 Project (Robertson et al., 2017), these approaches significantly underestimated the wave-induced floater motions at the natural frequencies outside the linear wave-excitation region. These results suggest that better models are needed for the hydrodynamic coefficients for nonlinear wave excitation. In the present work, the focus is on the added mass or damping coefficient for different motion amplitudes and periods.

The hydrodynamic coefficients in still water are characterized by two parameters: the motion amplitude and period. The nondimensional parameters are then the Keulegan-Carpenter (KC) number and the Stokes number β. Alternatively, one of the control parameters can be replaced by the Reynolds number (Re = KC·β).

Cozijn et al. (2005) performed experiments with a buoy with a skirt to investigate the heave, roll and pitch damping and found that the heave and pitch damping contain linear and quadratic components, where KC is in the range of 2–5 and β is from 76,923 to 200,000. Moreno et al. (2015), Philip et al. (2019) and Nallayarasu et al. (2014) experimentally investigated the hydrodynamic coefficients of heave plates on a spar platform at small KC (0.2–1) and high β (up to 31,250) values. The added mass and damping increased with KC number, independent of

* Corresponding author.
E-mail address: haoran.li@ntnu.no (H. Li).

https://doi.org/10.1016/j.oceaneng.2021.109130
Received 8 December 2020; Received in revised form 24 March 2021; Accepted 5 May 2021

frequency except for the increasing damping coefficients towards larger frequency at higher frequencies. For the hydrodynamic coefficients of heave plates of a semi-submersible FWT, Lopez-Pavon et al. (2015) also confirmed there is a relatively weak dependence on oscillation frequencies, and a large dependence on KC number, considering KC from 0.3 to 0.86 and Re from 79,695 to 446,294.

Model tests are the main means to study the hydrodynamic characteristics of FWTs, but due to limitations of the test conditions and accuracy of the test equipment, the conclusions of Chua et al. (2005) are not completely consistent with the results of Tao and Dray (2008) when investigating the effect of oscillation frequency on the damping of heave plate under similar KC (0.2–1.2) and β (16,000-160,000) values. Therefore, a series of numerical studies of hydrodynamic coefficients of FWT have been conducted.

Based on offshore oil and gas industry experience, Borg et al. (2013) and Lefebvre et al. (2012) suggested that the additional damping ratio generated by the vortex shedding is from 10% to 15%. Lopez-Pavon et al. (2015) computed, with a CFD commercial code (ANSYS CFX) and frequency domain panel method (WADAM), the hydrodynamic characteristics on heave plates of a semi-submersible FWT, and found added mass and damping were largely dependent on the motion amplitude. Furthermore, WADAM did not predict the increased added mass due to the edge of heave plates, especially for larger KC values. Bozonnet et al. (2015) used CFD tool OpenFOAM to calibrate and validate added mass and drag coefficients for a platform encompassing heave plates, where KC is in the range of 0.36–1.07 and β is from 8.80E+07 to 2.77E+08. The added mass was found to be slightly larger than the one predicted by potential flow theory and viscous effects were predominant in the damping term. The influence of different shapes of heave plates on hydrodynamic coefficients at small KC value (0.06–0.25) with β = 1.1E+08 were investigated by Wang et al. (2020). The results showed the added mass coefficient increases with KC number whereas the damping coefficient decreases with KC number for all types of heave plates. Zhang et al. (2018) examined the hydrodynamic coefficients of multiple heave plates by large eddy simulations with volume of fluid method and found that an accurate simulation of the unsteady flow separation around the sharp edges of the heave plates was essential for accurately predicting the drag coefficient.

The above numerical simulations studied the hydrodynamic coefficients using forced oscillation tests; free decay is another approach to estimate the hydrodynamic damping around the natural periods. Burmester et al. (2017, 2020b) investigated the surge decay of a moored semi-submersible FWT using CFD methods. The results showed the linear damping was largely influenced by the free surface and coupled motions increased the linear and quadratic damping slightly. Dunbar et al. (2015) compared the discrepancy of heave and pitch decay of a semi-submersible FWT between CFD methods and engineering tools and found the discrepancy is associated with Reynolds-number-dependent viscous effects.

Most existing studies focus on the hydrodynamic characteristics associated with one cylindrical column attached with a very thin heave plate. That is not completely consistent with the configuration of a semi-submersible FWT whose heave plate has a certain thickness (Robertson et al., 2016). The possible mutual effects of different columns have not been considered in the studies of one cylindrical column. In addition, little attention has been paid to the hydrodynamic characteristics at large KC value and longer period, such as natural periods of rigid-body motions of FWTs. Therefore, it is interesting to examine the hydrodynamic characteristics of a semi-submersible FWT at different KC numbers around the natural periods of rigid-body motions and to understand the variations of hydrodynamic characteristics among different columns.

In this study, a CFD model of a semi-submersible FWT is validated against experimental measurements including free decay and forced oscillation in surge. Then, several forced oscillations with different motion amplitudes around the surge, heave and pitch natural periods are performed using the validated numerical model to identify the added mass and damping coefficients on the whole floater. In addition, hydrodynamic characteristics on each column are extracted to better understand the effects of the multimember arrangement of the semisubmersible. Meanwhile, a potential flow model is used to estimate the added mass and damping coefficients and compare with the CFD model. The objective of this paper is to provide improved knowledge about the hydrodynamic characteristics of a semi-submersible FWT that can be potentially applied in engineering tools.

The organization of this paper is as follows. Section 2 describes the experimental setup. The CFD tool is described in Sec. 3 together with an introduction of the frequency domain panel method in WADAM based on potential flow theory. Numerical results of surge, heave and pitch decay are compared to the experimental data in Sec. 4, while the added mass and damping estimated by the forced oscillations are analyzed in Sec. 5. Conclusions are drawn in Sec. 6.

2. Experiment set up

In the present work, experimental data are from Phase I of the Offshore Code Comparison Collaboration, Continued, with Correlation, and unCertainty (OC6) project (Robertson et al., 2020b). The experiments were conducted in the concept basin of the Maritime Research Institute Netherland (MARIN) for the OC5-DeepCwind semi-submersible floater (Robertson et al., 2016) at 1:50 scale. The right-handed coordinate system used here originates at the center of the floater at the still water line, with positive y towards the starboard column, and z upward. All data and results are given at full scale in this paper, except when explicitly mentioned.

For the configuration of free decay shown in Fig. 1, the wind turbine was removed, but the inertial properties of the floater with tower correspond to the total inertial properties of OC5 system. The mooring system was replaced with 3 taut-spring-lines to reproduce the equivalent linear response behavior of the original catenary system. Robertson et al. (2020a, 2020b) provide the dimensions and structural properties of the platform and the configuration of the mooring lines. The global motions, including surge (x-displacement), heave (z-displacement) and pitch (y-rotation), were measured. The initial offsets for the surge, heave and pitch decay are given in Table 1.

For forced oscillation, the wind turbine and tower were removed, and the floater was attached to the carriage through a frame (Fig. 2). The floater was forced to oscillate in the surge (x-direction). Total forces on the floater were measured using a six-component gauge installed between the frame and floater. The details of the forced oscillation tests are provided in Table 2. Assuming the frequency of the radiated wave is the oscillation frequency, the length of the radiated wave can be obtained by the dispersion relation. The ratios between oscillation amplitudes (A) and radiated wave lengths (L) are given in Table 2.

3. Numerical model

3.1. CFD model

High-fidelity numerical simulations are performed with the open-source CFD toolbox OpenFOAM (Weller et al., 1998). The multiphase interDyMFoam solver is a fluid-structure interaction solver, where the Navier-Stokes and 6-degree of freedom (DOF) equations are solved in a coupled manner. The standard interDyMFoam with wave absorption toolbox waves2Foam (Jacobsen et al., 2012) is referred to as the waveDyMFoam solver, which is applied in the current research.

3.1.1. Governing equations

The waveDyMFoam solver utilizes the two-phase incompressible Reynolds-averaged Navier–Stokes equations (RANS) to compute the fluid-structure interaction. The governing equations consist of a mass and a momentum conservation equation, expressed as:

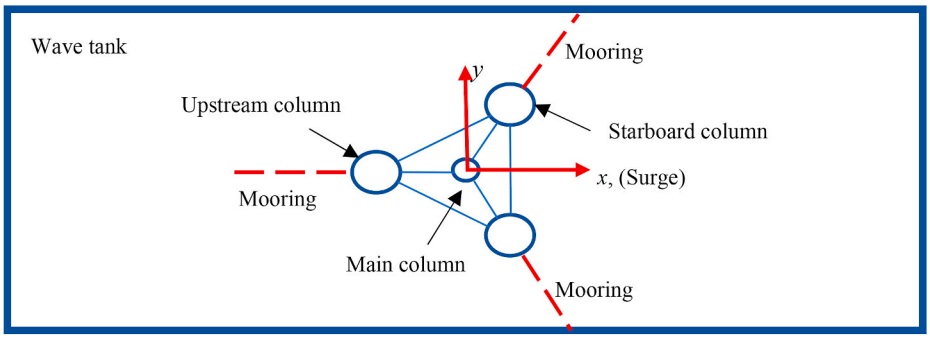

Fig. 1. The free decay configuration.

Table 1
Specifications for free decay tests in the experiments.

Load case	Mode	Initial offset
LC1.1	Surge	−1.86 m
LC1.2	Heave	−1.06 m
LC1.3	Pitch	−2.21°

$$\frac{\partial u_i}{\partial x_i} = 0 \tag{1}$$

$$\frac{\partial \rho u_i}{\partial t} + \frac{\partial \rho u_j u_i}{\partial x_j} = -\frac{\partial p^*}{\partial x_i} + F_{b,i} + \frac{\partial}{\partial x_j}\left[\mu_{eff}\frac{\partial u_i}{\partial x_j}\right] \tag{2}$$

where u_i $(i = x, y, z)$ are the fluid velocity in Cartesian coordinates, ρ is the fluid density, p^* is the pressure in excess of the hydrostatic pressure, $F_b$is the external body force including the gravity and mooring forces, and μ_{eff} is the effective dynamic viscosity.

The interface between air and water is tracked by the volume of fluid (VOF) method (Hirt and Nichols, 1981). The local fluid density ρ within a computational cell is calculated by the volume fraction α: for water $\alpha = 1$, for air $\alpha = 0$, and $0 < \alpha < 1$for all the intermediate values. The effective dynamic viscosity μ_{eff} is obtained by the sum of a calculated value based on the volume fraction and an additional turbulent dynamic viscosity $\rho\nu_t$:

$$\rho = \alpha\rho_{water} + (1-\alpha)\rho_{air} \tag{3}$$

Table 2
Specifications for surge forced oscillation in the experiment. L represents the wavelength of a linear wave at the oscillation period.

Load case	Amplitude, A(m)	Period (s)	A/L
LC2.1	30.07	104.5	1.75E-3
LC2.2	9.54	31.2	6.21E-3
LC2.3	3.37	21.0	4.93E-3

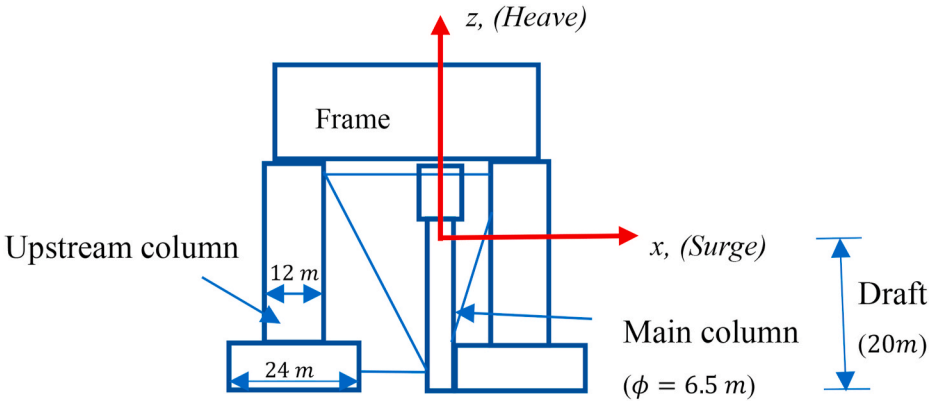

Fig. 2. The experimental configuration for forced oscillation.

Table 3
Specifications for forced oscillations in the CFD model.

Surge forced oscillation			Heave forced oscillation			Pitch forced oscillation		
T	A	A/L	T	A	A/L	T	A	A/L
(s)	(m)	(-)	(s)	(m)	(-)	(s)	(rad)	(rad/m)
200	1.91	3.06E-5	18.94	0.955	1.70E-3	37.04	0.068	3.17E-5
	3.82	6.12E-5		3.82	6.82E-3		0.136	6.35E-5
	7.64	1.22E-4		7.64	1.36E-2		0.273	1.27E-4
105	1.91	1.11E-4	17.30	0.955	2.04E-3	31.25	0.068	4.46E-5
	3.82	2.22E-4		3.82	8.17E-3		0.136	8.92E-5
	7.64	4.44E-4		7.64	1.63E-2		0.273	1.79E-4
66.67	1.91	2.75E-4	15.93	0.955	2.41E-3	27.03	0.068	5.96E-5
	3.82	5.50E-4		3.82	9.64E-3		0.136	1.19E-4
	7.64	1.10E-3		7.64	1.93E-2		0.273	2.39E-4

$$\mu_{eff} = \alpha\mu_{water} + (1-\alpha)\mu_{air} + \rho\nu_t \tag{4}$$

After the velocity field is known, the volume fraction is advanced in time by an advection equation:

$$\frac{\partial\alpha}{\partial t} + \frac{\partial u_i \alpha}{\partial x_i} + \frac{\partial u_{r,i}\alpha(1-\alpha)}{\partial x_i} = 0 \tag{5}$$

The last term on the left-hand side of Eq. (5), u_r, is introduced as an artificial compression term to decrease the smearing of the interface. It is only active in the vicinity of the interface, $0 < \alpha < 1$ (see Berberović et al. (2009) for details). A multi-dimensional flux limited scheme is applied to ensure stability.

The $k-\omega$ SST turbulence model (Menter et al., 2003b) is applied, consisting of a blending of the $k-\omega$ (Wilcox, 1998) and the $k-\varepsilon$ (Launder and Spalding, 1983) models. This model has shown good performance in simulating two-phase flow and wave elevation (Brown et al., 2014; Rahman et al., 2007), as discussed by Menter et al. (2003a). For the two-phase fluid in OpenFOAM, there is significant wave damping in the interface between air and water induced by increasing turbulent viscosity (Devolder et al., 2017; Fan and Anglart, 2020) when using this turbulence model. Hence, a modified waveDyMFoam solver is built to explicitly consider the variable density in the $k-\omega$ SST model (Fan and Anglart, 2020).

3.1.2. Boundary conditions

To solve the governing equations, boundary conditions are imposed on all the surfaces in the numerical domain. The general denomination of boundary surfaces is given in Fig. 3.

- At the inlet and outlet, the velocity, α field and the pressure are specified as zero normal gradient. The turbulent kinetic energy k and the specific dissipation rate ω are set as zero normal gradient.
- On the floater surface, a no-slip boundary condition (zero velocity) is specified, and the pressure is set as zero normal gradient. k is fixed at 1e-5 m^2/s^2 and ω is set as 1.0 1/s.
- For the atmosphere, the total pressure is set as zero and an atmospheric boundary condition is set for the velocity and α field. This means that air and water are allowed to leave the numerical domain, while only air is allowed to flow back in. k is fixed at zero and ω is specified as zero normal gradient.
- At the front, back and bottom of the domain, all the conditions are set as zero normal condition. Different k and ω values at floater and other boundaries are applied to accurately simulate the flow around the floater and reduce the influences of increasing turbulence viscosity around air-water interface.
- For the free decay, the displacement of the floater is calculated based on the total forces, while a prescribed sinusoidal displacement is applied for the forced oscillation. In addition to the forced surge oscillations in the experiment (Table 2), forced oscillations with different motion amplitudes (A) and periods (T) are carried out in the CFD model following Table 3. The displacements of other boundaries are set to zero.
- A continuous wall function based on Spadling's law (Dudley Brian, 1961) switching between low and high Reynolds numbers is implemented for the turbulent viscosity.

As in Table 2, the ratios between oscillation amplitudes (A) and radiated wave lengths (L) are also given in Table 3.

3.1.3. Relaxation zones

The Waves2Foam toolbox provides the relaxation zones (Region I and II in Fig. 3) to minimize the reflected wave from the inlet and outlet boundaries. Rectangular relaxation zones are defined in this work. See Bruinsma's work (Bruinsma et al., 2018) for details.

3.1.4. Coupling of Navier-Stokes/6-DOF solver

A partitioned fluid-structure model is applied to simulate the flow-dependent motion of a floating structure in OpenFOAM. Total forces on the body are calculated by solving the RANS equations for fluid and 6-DOF motion equations are used to obtain the rigid body motion. The stability of solutions can be ensured with a tighter coupling between fluid and motion solver. OpenFOAM provides two different methods: an under-relaxation and a predictor-corrector method (Ferziger et al., 2002). Based on Bruinsma's work (Bruinsma et al., 2018), the predictor-corrector method is more effective at eliminating the oscillations in the force profile. In order to reduce the computational time, the fixed number of subiteration loops to correct pressure in the predictor-corrector method is replaced with a quite small tolerance (10^{-8} Pa) when solving the pressure in this paper. No significant oscillation is seen in the resulting forces (shown in later sections of the paper, i.e. Fig. 11 in Section 5.1.1).

A deforming mesh technique is employed to conform to the moving boundary of the floater. For the free decay, the solver allows for specification of an innerDistance and an outerDistance. The mesh nodes within innerDistance move with the floater, while the mesh nodes between innerDistance and outerDistance morph. No morphing occurs for the mesh nodes outside the outerDistance. The solver of the forced oscillation uses a diffusivity function to control how the mesh morphing is distributed: farther away from the floater, there is less mesh morphing. The diffusivity function is the square of the inverse distance between the floater and mesh position.

The restraints for the floater are implemented by a linear spring without considering interaction with the fluid. The spring is given a simple constant stiffness and a rest length without any damping. The force in the spring follows Hooke's law. When the length of spring is equal to the rest length, the force in the spring is zero.

3.1.5. Computational domain

The floater at scale 1:50 was built in the numerical wave tank, mimicking the experimental set-up. The same coordinate system is also used in the CFD model, as shown in Fig. 4. The width (3.72 m, model scale) and water depth (3.6 m, model scale) of the numerical wave flume are equal to those of the experimental facility. The length of numerical wave tank should be long enough to dissipate the reflected waves from the boundaries. For the heave and pitch decays, the length is 4 m (model

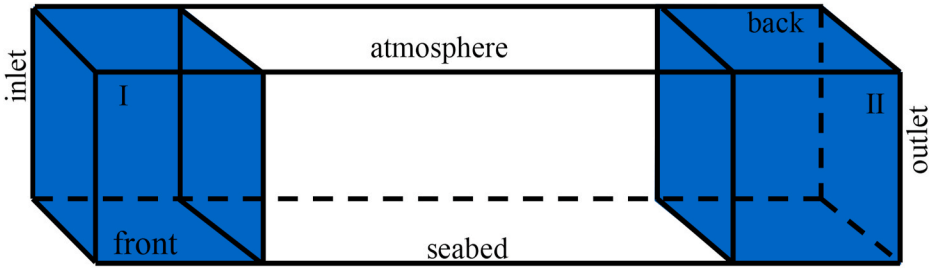

Fig. 3. Schematic representation of computational domain.

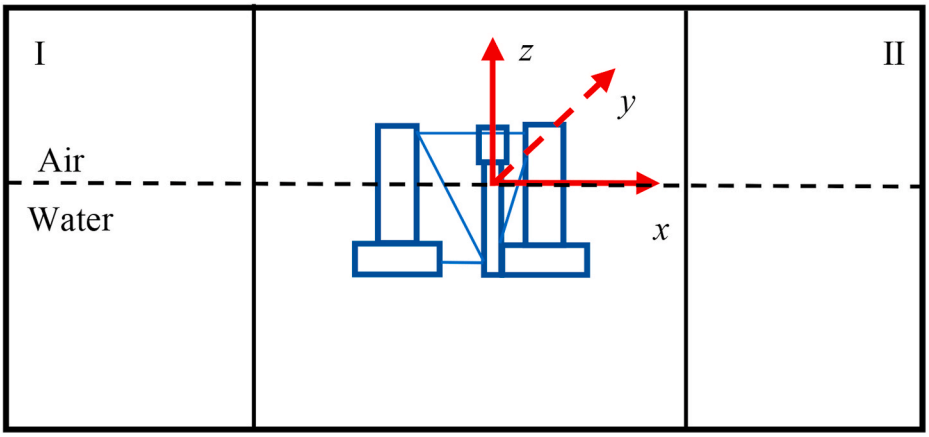

Fig. 4. Overview of the numerical wave tank with a semi-submersible FWT.

scale). Considering the longer period of surge decay and relatively larger amplitudes of the forced oscillations in surge, the length increases to 8 m (model scale). Half of the computational domain consists of the relaxation zones. In addition, the height of the air regime is set to 1 m (model scale). Fig. 4 shows a plan view of the numerical wave tank with floater which is placed at the origin of the numerical domain.

3.1.6. Temporal and spatial discretization

The Courant-Friedrichs-Lewy condition is implemented for the temporal discretization. A maximum Courant number of 0.3 is set to determine each time step.

Based on the finite volume method, the computational domain is discretized into finite regions in space known as cells where the conservation principles are applied. The size of a background cell in all the directions is 0.1 m (model scale) after discretization. Thereafter, the mesh needs to be refined towards the floater and free surfaces. 10 viscous layer cells adjacent to the floater surface are generated. An example of the mesh topology is shown in Fig. 5. Three different meshes used for the mesh convergence studies in the heave decay (LC1.2) are summarized in Table 4.

The time series of heave motions with different mesh sizes are compared in Fig. 6. A small difference is noticeable. Table 5 compares the reduction in the amplitude ("amplitude drop") and the duration of the first cycle. The numerical solution is converging with decreasing mesh size. The medium mesh (M2) is selected for the following simulations based on the small difference in results compared to the finest mesh, and the computational demands.

Table 4
Mesh size for mesh convergence study (model scale).

Mesh	Towards free surface	Towards floater
M1	2-2 level (0.025 m)	4-4 level (0.00625 m)
M2	3-3 level (0.0125 m)	4-4 level (0.00625 m)
M3	3-3 level (0.0125 m)	5-5 level (0.003125 m)

3.2. WADAM model

The frequency domain analysis for the hydrodynamic characteristics is conducted with WADAM (Veritas, 2010). A panel model (potential flow) is used for the columns and a Morison model is implemented for the braces. The radiation calculation results include the frequency-dependent linear added mass and damping coefficients. The braces contribute to the added mass through the inertial term of Morison's equation (added mass coefficient is 1.0), which is frequency-independent. The viscous contributions of the columns and braces to the damping are taken into account by including the drag term from Morison's equation.

Based on Morison's equation, the total viscous surge, heave force $F_{x,z-visc}(t)$ and pitch moment $M_{y-visc}(t)$ on the floater are evaluated by adding the viscous contributions of each column and brace.

$$F_{x,z-visc}(t) = \sum_i \frac{1}{2} \cdot \rho \cdot C_d \cdot A_{s,i} \cdot v_i(t) \cdot |v_i(t)| \tag{6}$$

$$M_{y-visc}(t) = \sum_i \frac{1}{2} \cdot \rho \cdot C_d \cdot A_{s,i} \cdot (R_i \cdot \theta_i(t)) \cdot |R_i \cdot \theta_i(t)| \cdot R_i \tag{7}$$

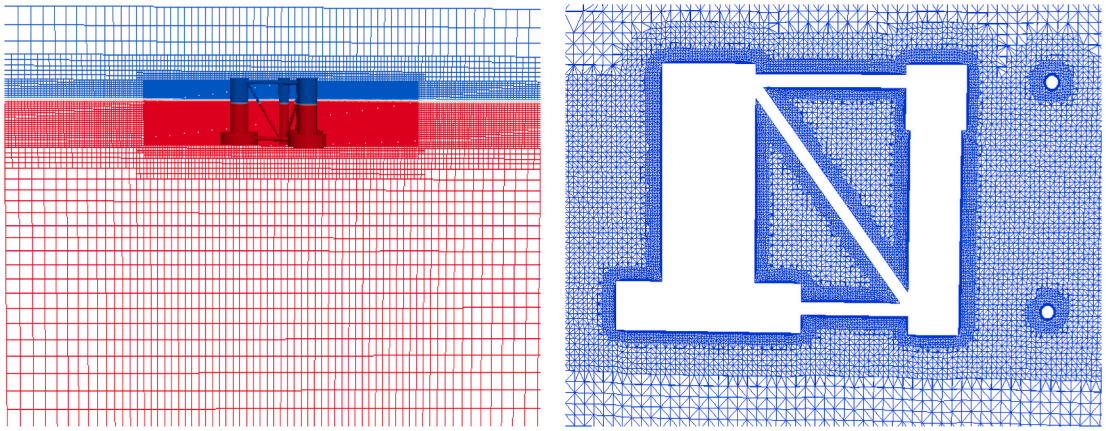

Fig. 5. Refined mesh towards the floater and the free surface.

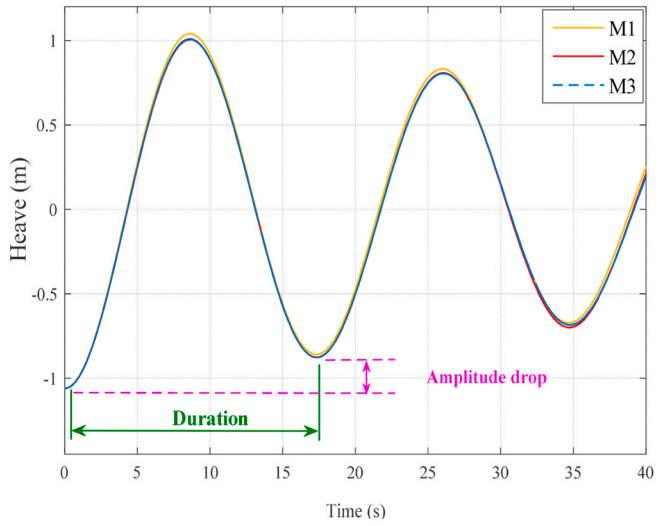

Fig. 6. Time series of heave motion with different mesh sizes in heave decay.

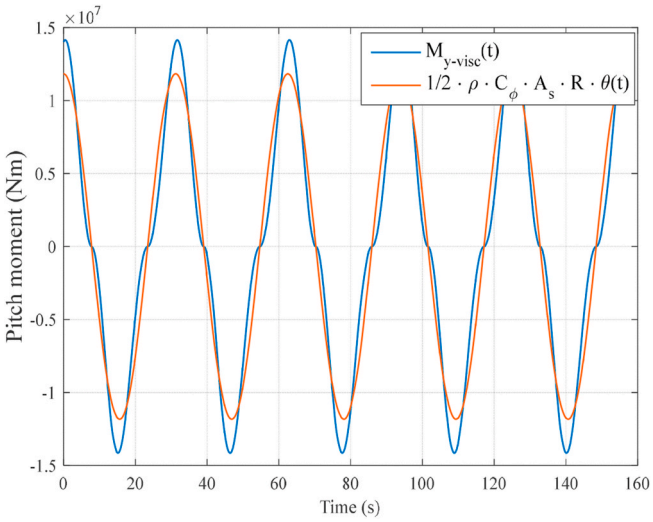

Fig. 7. Linearized total pitch moment, $T = 31.25$ s, $A = 0.136$ rad.

Table 5
Mesh for mesh convergence study.

Mesh	Amplitude drop (m)	Difference (%)	Duration (s)	Difference (%)
M1	0.2010	9.54	17.345	0.15
M2	0.1856	1.14	17.329	0.058
M3	0.1835	0	17.319	0

where ρ is water density, C_d is the quadratic drag coefficient in Morison's equation (0.744 in transverse direction from towing tests (Robertson et al., 2020b) and 2.48 in axial direction by matching experimental data in heave direction (Robertson et al., 2014)), $A_{s,i}$ is the projected area of each column or brace along x or z direction, $v_i(t)$ is the horizontal (surge force) or vertical (heave force) velocity and $\theta_i(t)$ is the angular (pitch moment) velocity at the center of wetted part of each column or brace and R_i is the distance between the center of the wetted part of column or brace and the origin of coordinate system.

Frequency-dependent linearized equivalent damping coefficients are then obtained for surge (C_{dx}), heave (C_{dz}) and pitch (C_φ) damping coefficients by fitting the time series of total viscous surge, heave force and pitch moment, minimizing the error, i.e. $\left|F_{x,z-visc}(t) - \frac{1}{2}\cdot\rho\cdot C_{dx,dz}\cdot A_s\cdot v(t)\right|$ and $\left|M_{y-visc}(t) - \frac{1}{2}\cdot\rho\cdot C_\varphi\cdot A_s\cdot R\cdot\theta(t)\right|$ with A_s being the project area of the whole floater along x or z direction, $v(t)$ being the horizontal or vertical velocity and $\theta(t)$ being the angular velocity at the center of wetted part of the whole floater and R being the distance between the center of wetted part of the whole floater and the origin of coordinate system. An example is shown in Fig. 7. These coefficients depend on two fundamental non-dimensional parameters (KC number and the Stokes number β) that are defined as

$$KC = \frac{2\pi A}{D} \tag{8}$$

$$\beta = \frac{D^2}{\nu T} \tag{9}$$

where D is the diameter of each column and ν is the kinematic viscosity of water.

In the present work, only the diagonal terms in the damping matrix are investigated, i.e. the total viscous surge forces are estimated due to surge motions but not the coupling between surge and pitch motions. Furthermore, different contributions in the WADAM model are investigated, as summarized in Table 6.

4. Free decay tests

Free decay tests are used to determine the natural periods and damping of the rigid body motions. In the current work, free decay tests in surge, heave and pitch (Table 1) were carried out in the experiments and numerical simulations. Assuming that there is no coupling among motions in different DOFs, a typical motion equation of a free decay test in calm water considering linear stiffness and nonlinear damping can be written as follows (Chakrabarti, 1994):

$$(m+a)\ddot{X} + B_1\dot{X} + B_2\dot{X}\left|\dot{X}\right| + KX = 0 \tag{10}$$

where X, $\dot{X}$ and $\ddot{X}$ are the motion, velocity and acceleration for the surge, heave or pitch motion. m is the mass or mass moment of inertia in pitch of rigid body and a is the added mass or mass moment of inertia in pitch. B_1 and B_2 are the linear and quadratic damping coefficients, respectively. K is the restoring coefficient.

Natural periods are estimated as the mean duration between two consecutive peaks or troughs. The damping ratio (ξ^*) relative to the critical damping is based on the logarithmic decrement (δ) for each cycle:

$$\delta = \ln\frac{x_n}{x_{n+1}} \tag{11}$$

where x_n and x_{n+1} are two consecutive peaks or troughs. The damping ratio is then calculated as:

$$\xi^* = \frac{1}{\sqrt{1+\left(\frac{2\pi}{\delta}\right)^2}} \tag{12}$$

In some cases, especially for small motion amplitudes, there are large variations in the damping ratio.

From the method of equivalent linearization, the damping ratio can

Table 6
Overview of different contributions in WADAM.

	Added mass coefficient	Damping coefficient
WADAM1	Radiation added mass from panel model	Radiation damping from panel model
WADAM2	WADAM1 with contributions of braces	WADAM1 with contributions of Morison-type drag

be expressed as a function of the decay motion amplitude (X):

$$\xi^* = \frac{B_1 + B_2 \frac{8\omega_n}{3\pi} X}{B_{cr}} \tag{13}$$

where ω_n is the oscillation frequency, $B_{cr} = 2 \cdot \sqrt{(m+a) \cdot K}$ is the critical damping. Based on Eq. (12) and Eq. (13), the linear and quadratic damping in the decaying motion can be obtained by the values of two consecutive peaks or troughs. As this estimate is sensitive to the magnitude of the peaks (or troughs), the best signal mean value is subtracted from the original decaying motion by minimizing the linear regression error (sum of squares).

4.1. Surge decay test

The surge decay results are presented in Fig. 8. The difference of motion amplitude between CFD simulation and experimental data is small at the beginning of the simulation, but increases with time. The comparison of damping ratio shows the surge decay is less damped in the CFD model. Furthermore, for large surge amplitude (>0.6 m), the linear component (given by the intercept) dominates. The linear damping estimated by the CFD model is approximately 30% smaller than the one predicted in the experiment. This large difference might be caused by the following reasons.

In the experiment, taut-spring-lines are connected with the floater by the pulleys (Robertson et al., 2020b). Some sources of mechanical friction, such as the damping between spring lines and pulley, are not quantified and are not considered in the CFD model. This mechanical friction may be the reason for the upturning tail in the damping ratio at small surge amplitudes (<0.6 m) in the experiment. There are also uncertainties related to performing a single experimental test. Furthermore, the post-processing method is important: the difference might be up to 10% when comparing the damping estimated by a least-squares approach and the classical peak-to-peak analysis (Burmester et al., 2020b).

The surge natural periods are compared in Table 7. Compared to the large difference of the linear damping, the difference in the natural periods is small. There is significant uncertainty in the mooring line axial stiffness (Robertson et al., 2020a): considering the upper limit of the mooring system stiffness would result in a surge natural period of 105.14 s in the CFD simulations. The uncertainty in measured motion is estimated as 5 mm full scale in the experiments; additional uncertainties exist in the mass and geometry of the model (Robertson, 2017).

4.2. Heave decay test

The comparisons of heave decay are presented in Fig. 9. The motion amplitudes between experiment and CFD model are in close proximity of each other. The comparison of damping ratio confirms that the heave damping at the small heave amplitude (<0.5 m) shows more linear behavior, while the damping becomes nonlinear as the heave amplitude increases. Compared to the experiment, the CFD model captures more linear damping (given by the intercept) and less quadratic damping (given by the slope). Despite the small difference in damping, the CFD model shows good correspondence with the experiment in predicting the heave natural period (within 0.4%) as presented in Table 7.

Table 7
Natural periods obtained from experiments and CFD simulations.

Mode of Motion	Experiment (s)	CFD (s)	Difference (%)
Surge	104.1	108.4	4.13
Heave	17.32	17.39	0.40
Pitch	31.29	31.07	0.70

4.3. Pitch decay test

For the pitch decay, interaction between pitch and surge motions was observed in the experimental results whereas no such interaction was found in the CFD simulation. Hence, motions at the surge natural frequency are removed from the experimental signal by a high-pass filter with a 0.015 Hz cut-off frequency. The filtered experimental pitch motion is presented in Fig. 10 together with the original CFD results. The CFD simulation captures both the period and damping well. Linear damping dominates the pitch damping, although the overall damping level shows large variations.

In conclusion, the CFD model is generally able to reproduce the natural periods and damping levels of the semi-submersible FWT floater. Better correspondence is observed in the heave and pitch decay tests with shorter natural periods. For the surge decay with longer period, there are some differences between CFD simulations and experimental measurements. Similar differences are also found in other work (Burmester et al., 2020a, 2020b, 2020b). Nevertheless, these differences are considered acceptable, given the differences between the experimental and numerical models and the uncertainties.

5. Forced oscillation tests

In the forced oscillations, harmonic motion is imposed on the floater. The position of the floater is:

$$X(t) = A \sin(\omega t) \tag{14}$$

where $X(t)$ represents surge motion along the x axis, $x(t)$, heave motion along the z axis, $z(t)$, or pitch motion around y axis, $\theta(t)$. For pitch, the center of rotation is located at the origin of the coordinate system. A is

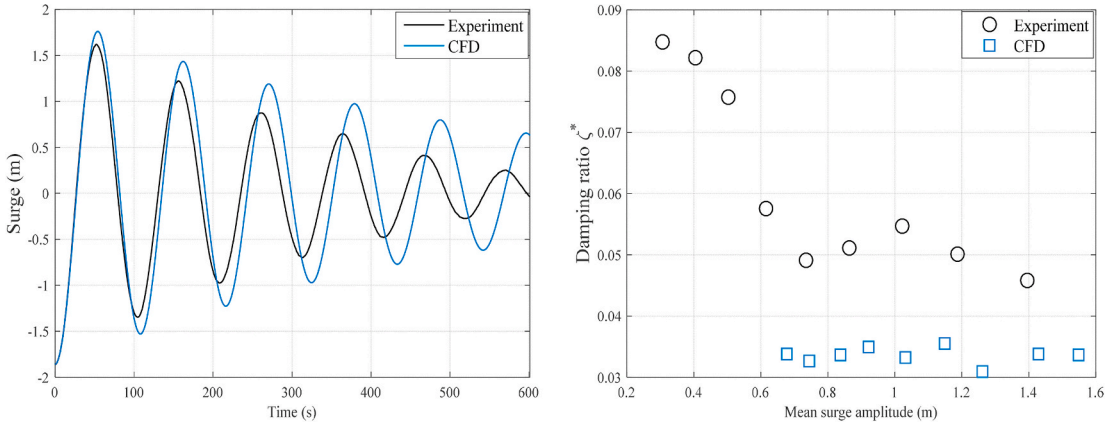

Fig. 8. Surge decay (left: original decaying surge motion, right: surge damping ratio).

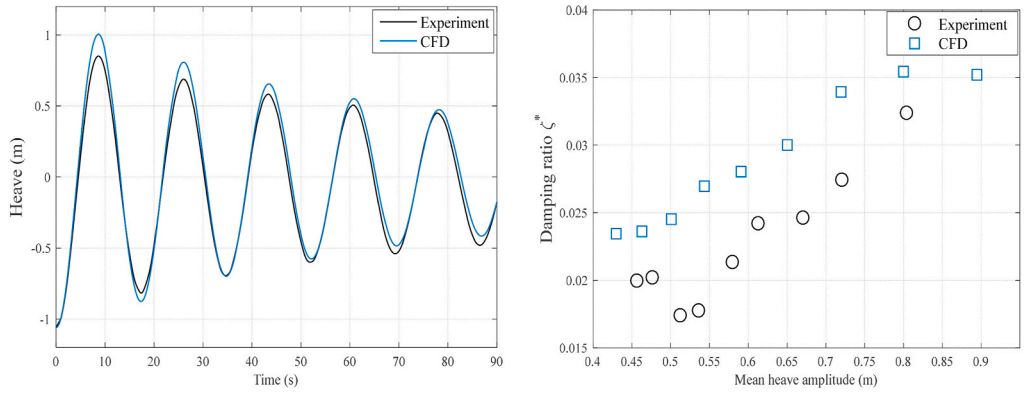

Fig. 9. Heave decay (left: original decaying heave motion, right: heave damping ratio).

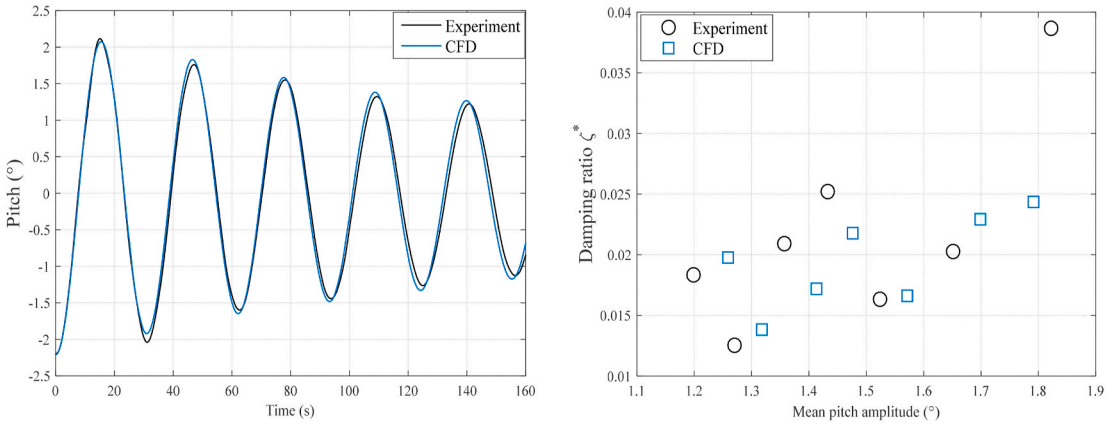

Fig. 10. Pitch decay (left: decaying pitch motion, Experiment: high-pass filtered results, right: pitch damping ratio).

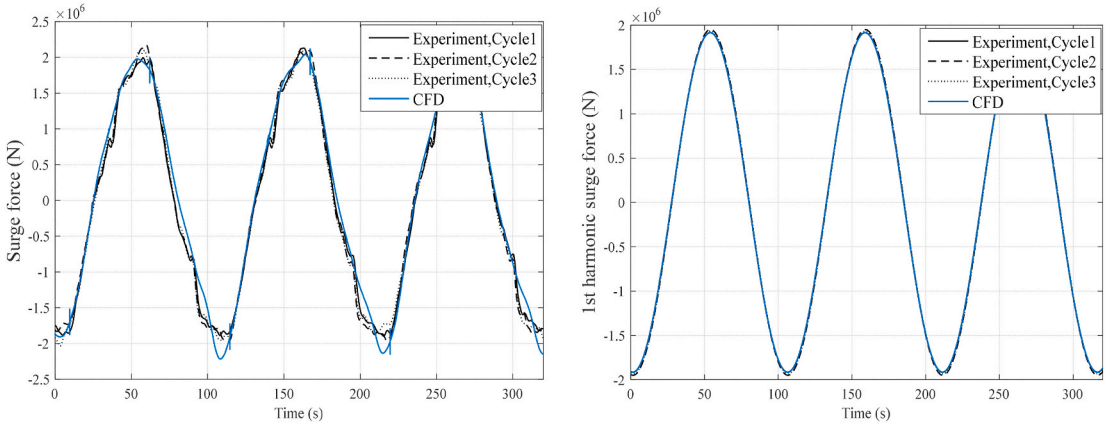

Fig. 11. Time series of surge force, LC2.1 (left: total hydrodynamic force, right: 1st harmonic hydrodynamic force).

the oscillation amplitude and ω is the oscillation frequency.

The hydrodynamic force on the floater, $F_H(t)$, is obtained by subtracting the inertial force, $F_I(t)$, and the linear hydrostatic restoring force, $F_K(t)$, from the measured or simulated total force, $F_T(t)$. That is:

$$F_H(t) = F_T(t) - F_I(t) - F_K(t) \tag{15}$$

The detailed expressions of inertial force and linear hydrostatic restoring force in the experimental and numerical results are given in Table 8. In the CFD simulation, the estimated total force is the integral of the hydrodynamic pressure along the surface of the floater, which does not include inertial forces. The linear hydrostatic restoring coefficient

Table 8
Motion, inertial force and linear restoring force in the experimental and numerical results. In the experiments, forced oscillations were only carried out in surge.

	$X(t)$		$F_I(t)$		$F_K(t)$	
Motion	Experiment	CFD	Experiment	CFD	Experiment	CFD
Surge	$x(t)$	$x(t)$	$-m\cdot\ddot{x}(t)$	0	0	0
Heave	N/A	$z(t)$	N/A	0	N/A	$K_{33}\cdot z(t)$
Pitch	N/A	$\theta(t)$	N/A	0	N/A	$K_{55}\cdot\theta(t)$

can be obtained from the variation of buoyancy loads due to small displacements in still water. Hence, the linear restoring coefficient in surge is zero and the linear restoring coefficient in heave, K_{33}, and in pitch, K_{55}, can be written as:

$$K_{33} = \rho g A_{wp} \tag{16}$$

$$K_{55} = \rho g V Z_B + \rho g \int_{A_{wp}} x^2 ds \tag{17}$$

where ρ is water density, g is the acceleration due to gravity, A_{wp} is the waterplane area, V is the volume of the floater, Z_B is the vertical coordinate of the center of buoyancy and the integral of Eq. (17) represents the waterplane area moment of inertia about y axis. In Eq. (17), the effect of weight is not included, because the estimated total force in the CFD simulation does not include the weight. For the main column, there is a ledge due to the large diameter for the upper part (see Fig. 2). When the heave oscillation amplitude exceeds the distance between the ledge and the still water line, varying waterplane area is used in the K_{33}.

The first harmonic component of hydrodynamic force, $F_H^{(1)}(t)$, or moment $M_H^{(1)}(t)$,with the same frequency as the motion, ω, is extracted and decomposed into in-phase and out-of-phase components:

$$F_H^{(1)}(t) = F_{H,\cos}^{(1)} \cdot \cos(\omega t) + F_{H,\sin}^{(1)} \cdot \sin(\omega t) \tag{18}$$

$$M_H^{(1)}(t) = M_{H,\cos}^{(1)} \cdot \cos(\omega t) + M_{H,\sin}^{(1)} \cdot \sin(\omega t) \tag{19}$$

The first-order hydrodynamic force or moment on the floater can be expressed based on the added mass and linearized damping coefficients as

$$F_H^{(1)}(t) = -\rho \cdot C_a \cdot V \cdot \ddot{X}(t) - \frac{1}{2} \rho \cdot C_{dx,dz} \cdot A_s \cdot \frac{8}{3\pi} \omega \cdot A \cdot \dot{X}(t) \tag{20}$$

$$M_H^{(1)}(t) = -C_a \cdot I \cdot \ddot{X}(t) - \frac{1}{2} \rho \cdot C_\varphi \cdot A_s \cdot R \cdot \frac{8}{3\pi} \omega \cdot A \cdot \dot{X}(t) \tag{21}$$

where I is the mass of moment inertia about the y axis.

Then, the added mass and linearized damping coefficients are found:

$$C_a = \frac{F_{H,\sin}^{(1)}}{\rho \cdot V \cdot \omega^2 \cdot A} \text{ or } C_a = \frac{M_{H,\sin}^{(1)}}{I \cdot \omega^2 \cdot A} \tag{22}$$

$$C_{dx,dz} = -\frac{F_{H,\cos}^{(1)}}{4/3\pi \cdot \rho \cdot A_s \cdot \omega^2 \cdot A^2} \text{ or } C_\varphi = -\frac{M_{H,\cos}^{(1)}}{4/3\pi \cdot \rho \cdot A_s \cdot R \cdot \omega^2 \cdot A^2} \tag{23}$$

where A is equal to 1 for the linear radiation damping considering the columns (WADAM1). The projected area for the pitch damping coefficient is the same as the surge damping coefficient. The estimated linearized damping coefficient from the CFD simulations includes both radiation damping and viscous damping.

5.1. Forced oscillations in surge

5.1.1. Validations against the experimental measurements

The numerical estimated total and first harmonic hydrodynamic forces under the forced oscillations in surge are compared against the experimental measurements in Fig. 11. The numerical solution remains stable and has a small oscillation at the larger surge force amplitude. Meanwhile, the total surge force reveals weak cycle-to-cycle variations. These fluctuations are also found in the experiments, considering the differences of total surge forces at the start (Cycle1), middle (Cycle2) and end (Cycle3) of the steady-state experimental data. Some possible reasons for these variations are the mechanical vibrations of the measuring equipment (for the experiment) and the nonlinear characteristics of hydrodynamic force and interaction between body motion with the radiated wave, which was produced by the previous motion. Furthermore, the numerically estimated first harmonic surge force is in good agreement with the experimental measurements (within 0.2%).

Fig. 12 compares the surge added mass and damping coefficients of the whole floater obtained from experiments and CFD simulations. The difference in the estimated added mass coefficient varies from 1.1% (T = 105 s) to 4.6% (T = 31.2 s). However, the estimated damping coefficient shows better agreement, and the largest difference occurs at T = 21 s (1.9%). Considering the ratios of oscillation amplitudes over radiated wave lengths (Table 2), the smaller the ratio is, the lower the radiated wave steepness is, the more dominant the linear effects are, and the better the estimated added mass and damping coefficients from CFD simulation approximate those from experiments.

In the experiments, the motion and forces were measured by different measurement devices. Whether the force and motion signals are measured synchronously or not is crucial for the estimations of added mass and damping coefficients. There is no accurate evaluation of time-lag between different signals in the experiments, so time lags of either 0.01 s (sampling interval in the experiments) and 0.02 s are used to investigate this effect. This estimated time lag is similar to the time lag observed in hybrid testing of a floating wind turbine (Sauder et al., 2016). The added mass and damping coefficients under motion-lead or force-lead are estimated and shown in the uncertainty bars of Fig. 12. The time-lag between motion and force has minor influence on the calculated added mass coefficients, but its impact on the calculated damping coefficients is more significant for shorter oscillation periods. The same trend is observed for the different time-lags.

Generally, good agreement is obtained between measured and numerically estimated hydrodynamic surge force and added mass and damping coefficients, which suggests that it is possible to reproduce the correct hydrodynamic characteristics at low oscillation frequency in the CFD model.

5.1.2. Forced oscillation in surge in the CFD model

Based on Eq. (8), the KC numbers of each column of floater under forced oscillations in surge in the CFD model are presented in Fig. 13. The KC numbers vary from 0.5 to 7.4 and β is from 2.11E+05 to 8.64E+06.

Fig. 14 compares the total surge added mass and linearized damping coefficients calculated from the CFD simulations and the values due to linear radiation considering the columns (WADAM1) and the contributions of Morison's added mass and drag terms on the braces (WADAM2). The CFD simulations lead to similar added mass coefficients for smaller amplitudes (1.91 m and 3.82 m). However, for the largest amplitude (7.64 m), the added mass coefficient is 2.7% smaller. This decrease is closely related with the variation of KC numbers on each column. More details can be found in the discussions about the added mass coefficients for different columns. Compared to the CFD model, potential flow theory (WADAM1) underestimates the added mass (up to 10%). Furthermore, the contribution of braces only accounts for 2.5 percent in the potential flow added mass (WADAM1 vs WADAM2). In addition, the results also highlight the weak dependency of added mass on oscillation period.

In the CFD simulations, the linearized damping coefficient decreases with oscillation amplitude and increases with oscillation period. Considering the definition of linearized damping coefficient in Eq. (23), the damping has opposite trend with the linearized damping coefficient. That means the faster the surge motion is, the larger the damping is. In the potential flow results, the radiation damping (WADAM1) is completely negligible with respect to the viscous damping (WADAM2). The linearized damping coefficient in the WADAM2 model is close to the quadratic damping coefficient (0.744) in Morison's equation. Compared to the CFD results, Morison-type drag coefficient based on the towing tests in WADAM2 underestimates the viscous damping.

The obtained surge added mass and linearized damping coefficients on individual columns are compared numerically in Fig. 15. Based on other research (Dütsch et al., 1998; Gao et al., 2020), the added mass

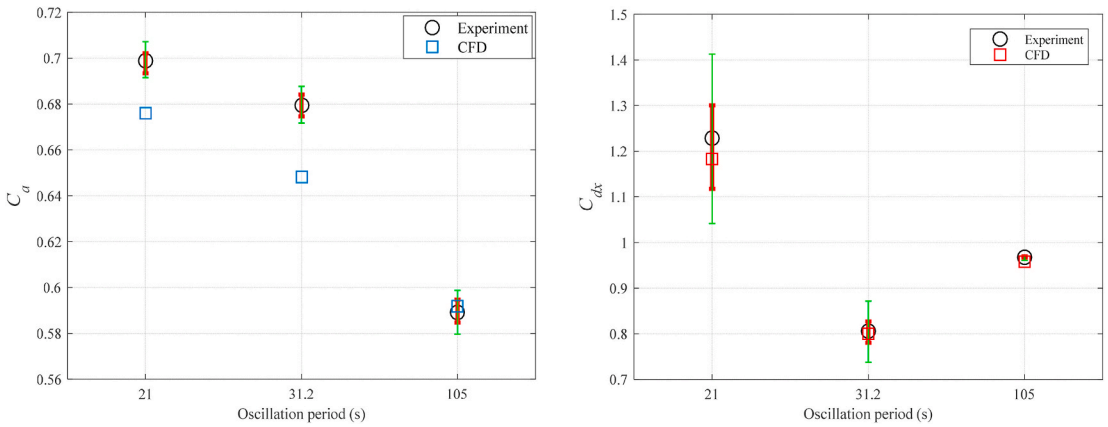

Fig. 12. Surge added mass and damping coefficients, LC2.1-LC2.3. Red and green uncertainty bars represent the influences of 0.01 s and 0.02 s (model scale) time-lags between different signals in the experiments, respectively. (For interpretation of the references to colour in this figure legend, the reader is referred to the Web version of this article.)

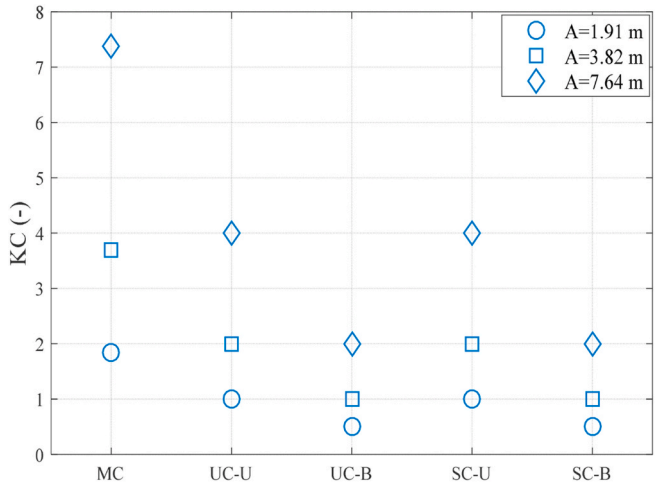

Fig. 13. KC numbers of each column under forced oscillations in surge (MC: main column, UC-U: upper part of upstream column, UC-B: heave plate of upstream column, SC-U: upper part of starboard column, SC-B: heave plate of starboard column. See Figs. 1 and 2 for the definitions of columns).

coefficient of a circular cylinder is weakly dependent on the KC number when KC < 3. For larger KC number, the added mass coefficient decreases as KC increases and achieves the minimum value around KC = 15. Then the added mass coefficient increases with KC. Hence, for the main column (KC > 2), the added mass coefficient decreases with increasing oscillation amplitude. For the upper part of column, the added mass coefficient has similar results (within 1%) under two smaller oscillation amplitudes (KC < 2), and significantly reduces for the largest amplitude (KC = 4). For the heave plates (KC < 2), the weak dependency of added mass coefficient on oscillation amplitudes seems to be valid for longer oscillation period (slow surge motion), but the added mass coefficient increases with KC for shorter oscillation period. All the changes are due to the variations of vortex pattern around the floater.

The computed hydrodynamic pressures on the aft (Point B) and starboard sides (Point A) of upper part of starboard column are shown in Fig. 16. The double frequency and negative mean value of hydrodynamic pressures on the starboard side show the occurrence of vortex shedding in the CFD simulations. Compared to the CFD results, potential flow predicts smaller added mass coefficient with a maximum difference of 15.6% (200 s, SC-B) except a larger added mass coefficient under largest oscillation amplitude for the upper part of columns (UC-U,SC-U). Additionally, the added mass coefficient on the starboard column is larger than the one on the upstream column, and this increase is more significant in the CFD simulations.

Dütsch et al. (1998) show that the drag coefficient decreases with increasing KC numbers for KC < 3. When 3<KC < 15, the drag coefficient is weakly dependent on the KC number. The same trends can be seen in the CFD simulations (Fig. 15). The linearized damping coefficient decreases as KC increases. However, for larger KC values, such as larger amplitude for the main column (MC) and upper part of upstream and starboard column (UC-U, SC-U), the variations of linearized damping coefficients over oscillation amplitude are quite small.

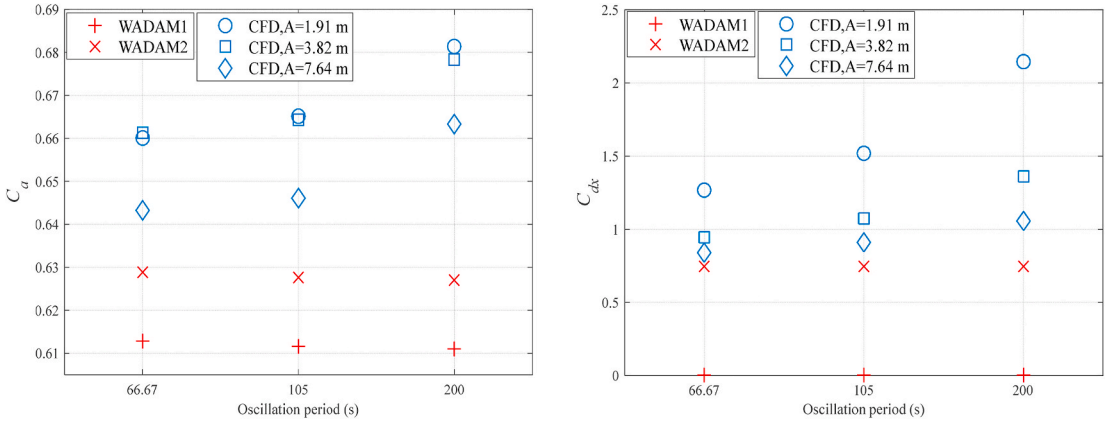

Fig. 14. Surge added mass and linearized damping coefficients for the whole floater.

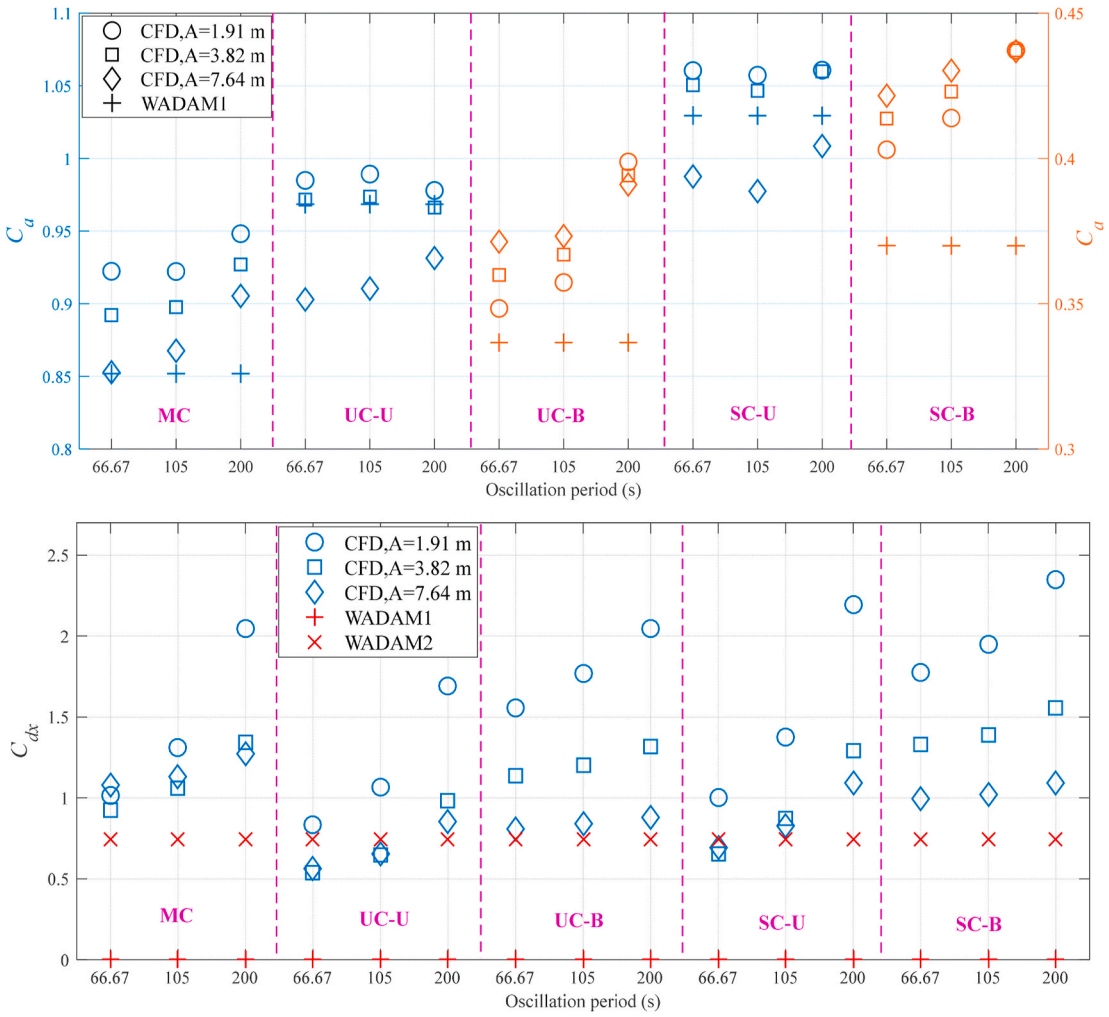

Fig. 15. Surge added mass and linearized damping coefficients for each column of the floater (MC: main column, UC-U: upper part of upstream column, UC-B: heave plate of upstream column, SC-U: upper part of starboard column, SC-B: heave plate of starboard column. See Figs. 1 and 2 for the definitions of columns. Top: The added mass coefficient of MC,UC-U and SC-U corresponds to the left *y* axis while the added mass coefficient of UC-B and SC-B corresponds to the right *y* axis. Bottom: The linearized damping coefficient of each column uses the left *y* axis.).

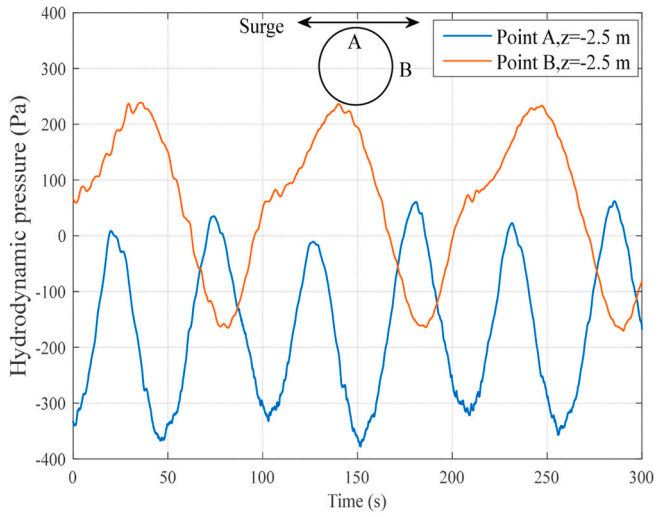

Fig. 16. Hydrodynamic pressures around upper part of starboard column, T = 105 s, A = 7.64 m.

Furthermore, the linearized damping coefficient of each column increases with oscillation period. The damping coefficient for each column in WADAM model has similar results as the total damping coefficient. However, the underestimation of viscous damping by Morison-type drag (WADAM2) does not seems to be valid for all comparisons. This also highlights the different drag coefficients instead of a uniform one should be applied in accurate estimations of viscous damping for each column. Furthermore, in the CFD simulations, the starboard column has a slightly larger damping compared to the upstream column. The shorter distance from the main column along the *x* direction and the effect of the portside column can explain this additional damping.

In order to validate whether there are consistent conclusions between free decay and forced oscillation or not, the durations of different cycles in the surge free decay are given in Table 9. The small variations in durations suggest that the motion amplitude has minor effect on the added mass, considering the maximum KC number is 1.8. Furthermore, from Fig. 8, the damping is also weakly dependent on the KC in the free decay, which is not consistent with conclusions in the forced oscillation.

Table 9
Durations of different cycles under the surge free decay in the CFD model.

	Cycle1	Cycle2	Cycle3	Cycle4	Cycle5
Duration (s)	108.6	108.1	108.2	108.3	108.6

The possible reason is that linear damping dominates for very small motion. However, when the mean motion amplitude in the free decay is close to the motion amplitude in the forced oscillation, the estimated added mass and damping are in good agreement, as shown in Table 10.

5.2. Forced oscillations in heave

For the forced oscillations in heave, the KC number is defined based on the heave plate diameter for the upstream and starboard columns. The corresponding KC numbers are presented in Fig. 17, ranging from 0.25 to 7.4. The β varies from 2.23E+06 to 3.62E+07.

The total heave added mass and linearized damping coefficients are presented in Fig. 18. The added mass coefficient increases with oscillation amplitude. For all cases, the calculated added mass coefficient from the CFD simulations is higher than the one derived from the potential flow theory (WADAM1), with a maximum increase of 32% (7.64 m). Similar results can be found in previously published research (Cozijn et al., 2005; Lopez-Pavon and Souto-Iglesias, 2015). A possible explanation for this increase is that the flow separation and the formation of eddies at the edge of heave plates for the large motion change the phase difference between the pressure and the motion of floater. The braces give minor contributions to the total added mass coefficient (within 2%). Finally, the added mass coefficient is independent of the oscillation period.

The linearized damping coefficient is independent of the oscillation period and decreases as the oscillation amplitude increases in the CFD simulations. By comparing WADAM1 and WADAM2, viscous damping dominates and the radiation damping is completely negligible. The difference of the computed linearized damping coefficient between WADAM1 and WADAM2 is close to the quadratic drag coefficient (2.48 by matching the experimental data) in Morison's equation, which underestimates the viscous damping.

The heave added mass and linearized damping coefficients among different columns are compared in Fig. 19. The added mass and linearized damping coefficients of the main column are much smaller than the upstream and starboard columns, even when dividing by the small diameter, which is related to the lack of a heave plate. For smaller oscillation amplitudes (0.955 m and 3.82 m), CFD and potential flow theory predict similar added mass coefficients for the main column, which seems to be independent of the oscillation period and amplitude. However, for the largest oscillation amplitude (7.64 m), the added mass increases sharply and shows significant dependency on the oscillation period. This is because the oscillation amplitude is larger than the distance between the ledge (see Fig. 2) and still water line (4.25 m) and the occurrence of flow separation and eddies at the ledge gives additional added mass. The overestimation for the linearized damping coefficient on the main column by Morison-type drag suggests that a smaller axial drag coefficient should be applied for the column without the heave plate.

The contribution of the heave plate is dominant for the heave forces, and the added mass and linearized damping coefficients for the upstream and starboard columns show similar trends as the total added mass and linearized damping coefficients. Furthermore, there are no significant differences between the upstream and starboard columns.

The consistency of conclusions based on free decay and forced oscillation in heave is also investigated. From Fig. 18, the radiation added mass gives a good estimate of the added mass with small heave motion. The heave free decay considers motion amplitudes which are smaller than the forced oscillations, and there is no significant change in the duration of different cycles during the decay (Table 11). From Fig. 9, the linear damping increases with the motion amplitude. Considering the definition of linearized damping coefficient in Eq. (23), the linearized damping coefficient decreases as the motion amplitude increases, which is the same conclusion as the free decay tests. Table 12 compares the estimated heave added mass and damping with similar motion amplitude in free decay and forced oscillation. The added mass agrees well, whereas the damping is quite sensitive to the motion amplitude.

Table 10
Comparisons of surge added mass and damping between free decay and forced oscillation in the CFD model.

	Free decay	Forced oscillation
Amplitude (m)	1.584	1.91
Added mass (kg)	8.98E6	9.23E6
Damping (Ns/m)	8.97E4	9.70E4

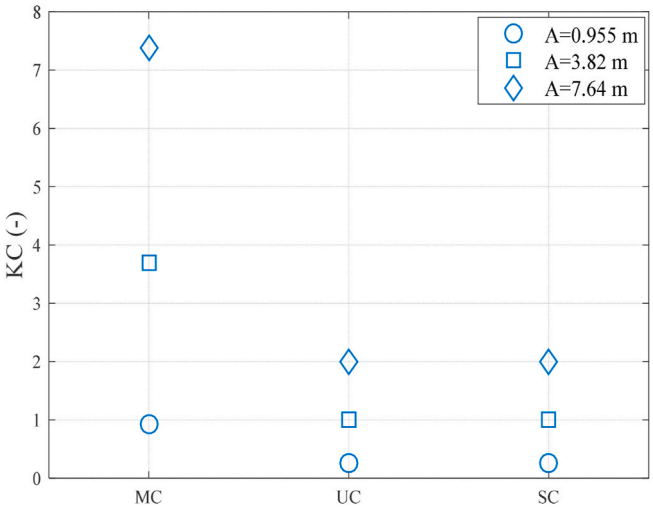

Fig. 17. KC numbers of each column under different heave forced oscillations (MC: main column, UC: upstream column, SC: starboard column. See Figs. 1 and 2 for the definitions of columns).

5.3. Forced oscillations in pitch

The total pitch added mass and linearized damping coefficients are compared in Fig. 20. For small pitch motion, the total added mass coefficient is independent of the oscillation period and increases slightly with oscillation amplitude. However, the total added mass coefficient decreases with oscillation period for the largest pitch motion (0.273 rad). A possible explanation is that complex vortex-vortex and vortex-column interaction can change the vortex pattern around the column for large pitch motions. There is a significant underestimation of the pitch added mass coefficient using potential flow theory. The contribution of braces to the total pitch added mass coefficient is less than 1%.

The pitch linearized damping coefficient decreases with the oscillation amplitude and shows a weaker dependency on the oscillation period. Furthermore, the viscous damping dominates and the radiation damping can be neglected (WADAM1 vs WADAM2). The applied Morison's drag coefficients by matching experimental data underpredict the viscous damping.

Since the mass distributions of each column are unknown, the mass of moment inertia about y axis (Eq. (22)) is calculated assuming the mass is uniformly distributed. The pitch added mass and linearized damping coefficients among different columns can be seen in Fig. 21. In the CFD model, the main column has some "openings" at the intersection with the braces where no pressure results are obtained. The loss of pressure at these openings leads to the negative added mass coefficient of the main column in the CFD simulations. In the potential flow calculation, the main column is considered as a closed cylinder. This effect on the added mass and linearized damping coefficients is shown in Table 13 with a difference in percentage from the results with braces. When the main column is built as a closed cylinder (without brace) in the CFD simulation, the added mass coefficient changes to positive (Table 13), but is also smaller than the potential flow solution presented in Fig. 21.

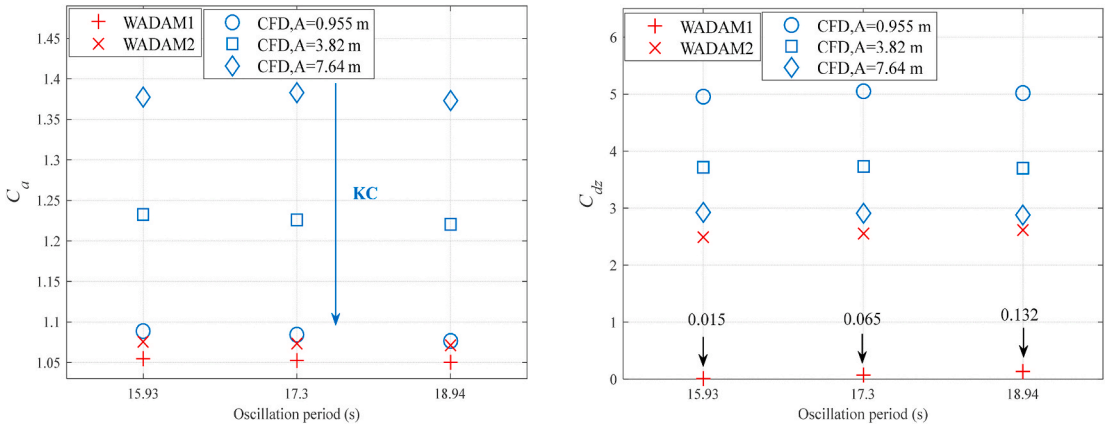

Fig. 18. Heave added mass and linearized damping coefficients for the whole floater.

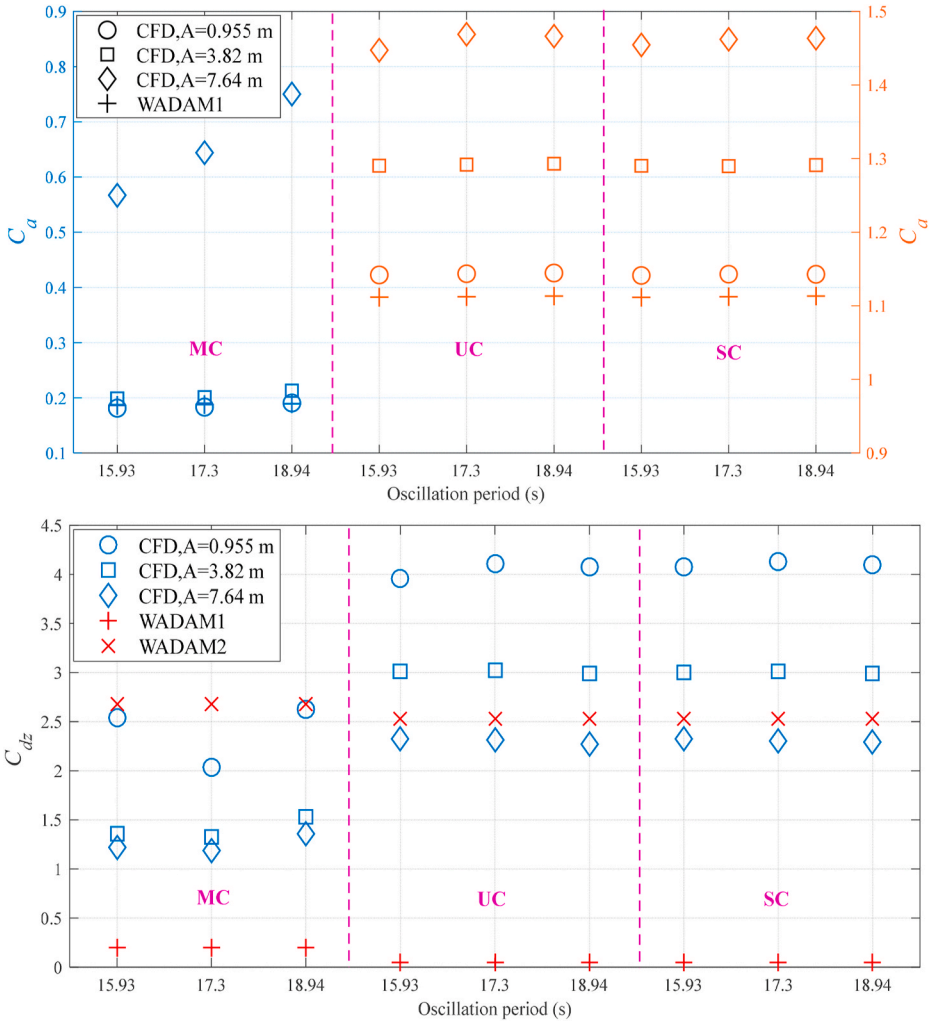

Fig. 19. Heave added mass and linearized damping coefficients for each column of the floater (MC: main column, UC: upstream column, SC: starboard column. See Figs. 1 and 2 for the definitions of columns. Top: The added mass coefficient of MC corresponds to the left *y* axis while the added mass coefficient of UC and SC corresponds to the right *y* axis. Bottom: The linearized damping coefficient of each column uses the left *y* axis.).

Table 11
Durations of different cycles under the heave free decay in the CFD model.

	Cycle1	Cycle2	Cycle3	Cycle4	Cycle5
Duration (s)	17.3	17.4	17.4	17.4	17.4

Furthermore, the added mass coefficient of the main column seems to be independent of the oscillation amplitude, but its magnitude increases with the oscillation period. The negative added mass coefficient of main column is useful to consider for further modification of potential flow results in order to better simulate local responses on the semi-submersible FWT. The interaction between heave plate and braces has

Table 12
Comparisons of heave added mass and damping between free decay and forced oscillation in the CFD model.

	Free decay	Forced oscillation
Amplitude (m)	0.894	0.955
Added mass (kg)	1.504E7	1.507E7
Damping (Ns/m)	7.439E5	9.046E5

minor influence on the added mass coefficient for the upstream and starboard columns (Table 13). The added mass coefficient of the upstream column has similar behavior as the total added mass coefficient because most of total pitch moment arises from the contribution of the upstream column. The added mass coefficient of the starboard column also shows similar trends as the total added mass coefficient except a slight decrease with the oscillation period for the smaller oscillation amplitude. Linear potential flow theory underestimates the added mass coefficient of upstream column, but overestimates the results for the main and starboard columns.

The pitch linearized damping coefficients of different columns (Fig. 21) appear to weakly depend on the oscillation period and decrease with the oscillation amplitude. Given both the magnitude of the linearized damping coefficient and the projected area (Eq. (23)), the upstream column contributes the most to the damping. The Morison-type drag coefficients by matching experimental data underestimate the viscous pitch damping. The interaction between columns and braces reduces the damping on each column (Table 13), with a minimum decrease of 0.59% for the upstream column and a maximum decrease of 31.44% for the main column.

Similar conclusions can be found between free decay and forced oscillations in pitch. The small variations of duration for different cycles (Table 14) in the pitch free decay are consistent with the constant added mass for small pitch motion in the forced oscillations in pitch. Furthermore, from Fig. 10, the linear damping increases with the motion amplitude. Considering the definition of linearized damping coefficient (Eq. (23)), the linearized damping coefficient decreases as the motion amplitude increases, which is the same conclusion as the forced oscillations. Table 15 compares the added mass and damping coefficient for the maximum mean pitch motion in the free decay and the minimum pitch motion in the forced oscillation. The estimated added mass is in good agreement whereas the calculated damping has a linear relationship with the amplitude.

6. Conclusions

In order to investigate the still-water hydrodynamic characteristics of the floater for a semi-submersible FWT, a series of free decay and forced oscillation tests have been conducted in experiments and in a CFD model. The focus is on long periods which are close to the natural periods for rigid body FWT motions. In the current work, the KC number varies from 0.25 to 7.4 and β is in the range of 2.11E+05 to 3.62E+07.

For the free decay, better correspondence can be found in the heave and pitch decay with shorter natural periods. However, for the surge decay with longer period, CFD underestimates the damping by 30% compared to the experiment. It is hypothesized that the additional damping between spring lines and pulleys, as well as coupling of rigid body motions increases the damping in the experiment. The uncertainty of experimental data and post-processing also contributes to this difference. Furthermore, the linear damping dominates the surge and pitch damping while quadratic damping is found in the heave damping due to the vortex shedding around the edge of heave plates. The estimated natural periods of the floater motion are in good agreement with ones calculated from the experiments (within 4.5%).

Forced oscillations in surge around the natural periods of surge, heave and pitch motion are firstly performed in the CFD model for validation. Compared to the experimental results, the maximum difference of 4.6% for the added mass coefficient and 1.9% for the damping coefficient suggest the CFD model can reproduce the correct hydrodynamic characteristics at low oscillation frequency. Next, the hydrodynamic characteristics of the whole floater and each column are analyzed using the CFD model. The results are compared with the results from the potential flow theory with Morison-type drag. The drag coefficients are determined by matching the experimental data.

For these long periods, the surge added mass coefficient seems to be independent of the oscillation amplitude for small surge motion (KC $<$ 2) and then decreases with the oscillation amplitude. A slight period dependency can be found in the surge added mass coefficient. Furthermore, the surge linearized damping coefficient increases towards longer period and smaller motion amplitude. The surge added mass and linearized damping coefficients on the starboard column are slightly larger than on the upstream column.

The heave added mass and linearized damping coefficients show, on one hand, a small dependence on the oscillation period and, on the other hand, a larger dependence with the oscillation amplitude. Most of contributions of added mass and linearized damping coefficients come from the heave plates. No difference can be found between the upstream and starboard columns.

A weak dependency of the pitch added mass coefficient on the oscillation amplitude and period is found for small pitch motion. However, the pitch added mass coefficient decreases with oscillation period for large pitch motion. The pitch linearized damping coefficient has similar behavior as the heave linearized damping coefficient.

The added mass coefficient derived from the CFD simulation is slightly superior to the one estimated by the potential flow theory in most cases. Viscous effects give an additional added mass. Regarding the

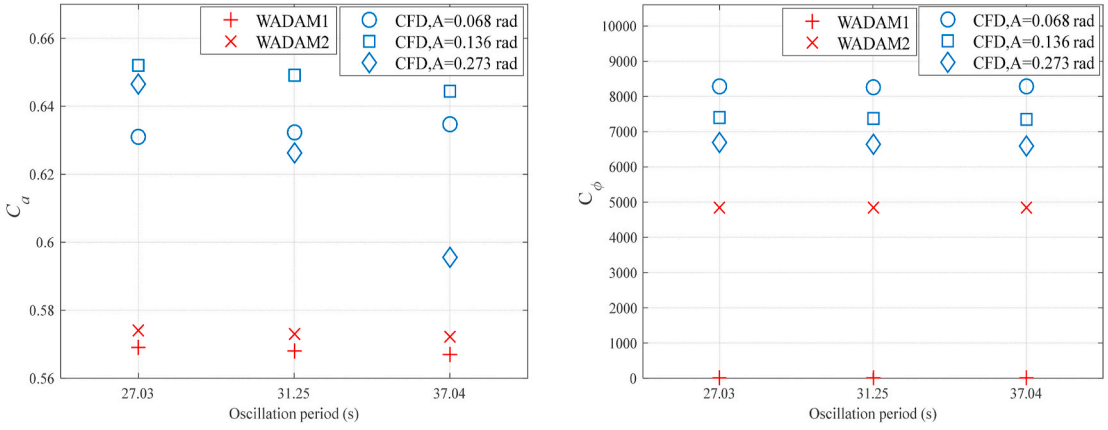

Fig. 20. Pitch added mass and linearized damping coefficient for the whole floater.

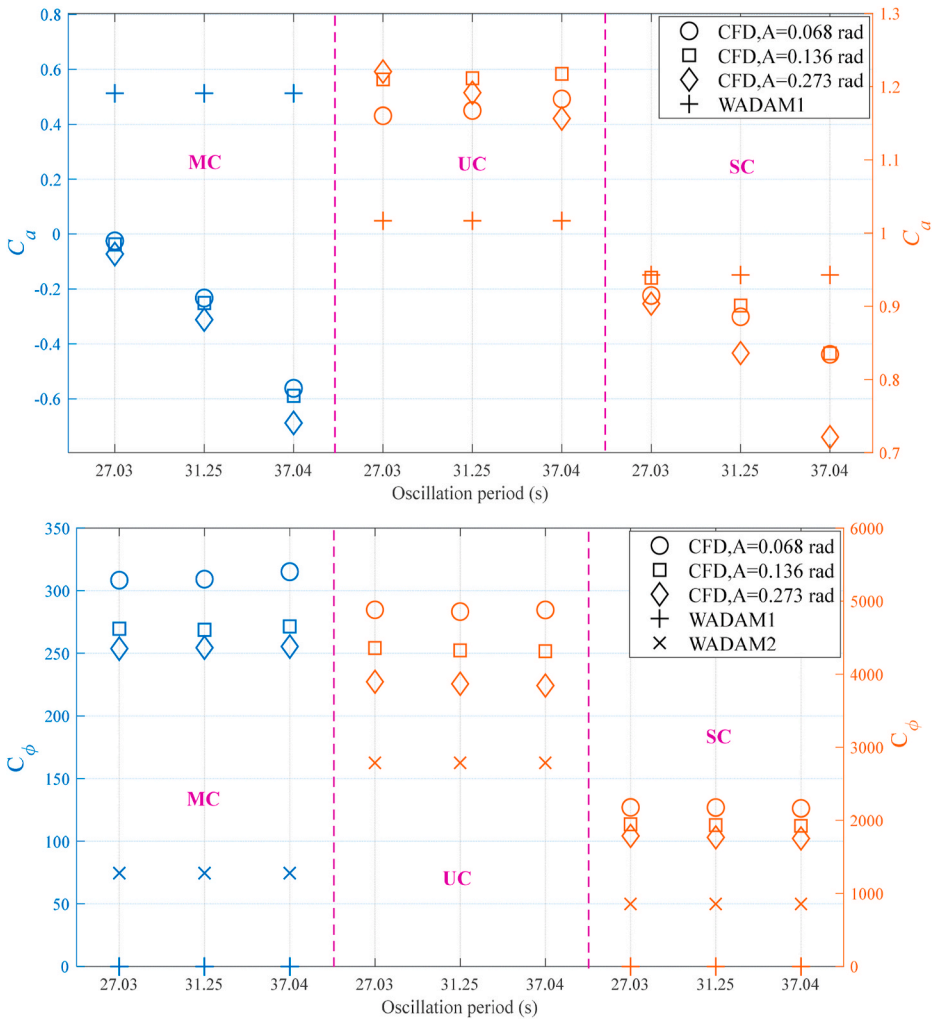

Fig. 21. Pitch added mass and linearized damping coefficients for each column of the floater (MC: main column, UC: upstream column, SC: starboard column. See Figs. 1 and 2 for the definitions of columns. The added mass and linearized damping coefficients of MC correspond to the left *y* axis while the added mass and linearized damping coefficients of UC and SC correspond to the right *y* axis).

Table 13
The effects of brace on the pitch added mass and damping coefficient on each column in the CFD simulations, T = 31.25 s, A = 0.136 rad.

		with brace	without brace	Difference (%)
Added mass coefficient	MC	−0.251	0.268	206.8
	UC	1.211	1.125	7.43
	SC	0.901	0.860	4.55
Linearized damping coefficient	MC	268.72	184.34	31.44
	UC	4326.5	4280.0	1.07
	SC	1934.0	1922.5	0.59

Table 14
Durations of different cycles under the pitch free decay in the CFD model.

	Cycle1	Cycle2	Cycle3	Cycle4	Cycle5
Duration (s)	31.1	31.1	31.1	31.0	31.1

damping, the radiation damping is completely negligible and the viscous damping from vortex shedding dominates. The accuracy of capturing the vortex shedding using Morison's drag force is sensitive to the drag coefficient.

Finally, free decay and forced oscillation tests give consistent conclusions about the trend of added mass and damping coefficients over the amplitude.

Table 15
Comparisons of pitch added mass and damping between free decay and forced oscillation in the CFD model.

	Free decay	Forced oscillation
Amplitude (rad)	0.031	0.068
Added mass (kgm^2)	8.817E9	8.533E9
Damping (Nm)	2.227E8	4.593E8

CRediT authorship contribution statement

Haoran Li: Conceptualization, Methodology, Software, Validation, Investigation, Formal analysis, Data curation, Writing – original draft. **Erin E. Bachynski-Polić:** Conceptualization, Methodology, Resources, Writing – review & editing, Supervision.

Declaration of competing interest

The authors declare that they have no known competing financial interests or personal relationships that could have appeared to influence the work reported in this paper.

Acknowledgements

The author Haoran Li gratefully acknowledges the financial support from China Scholarship Council (CSC). Computing time on Vilje is granted by the Norwegian Research Council (Program for Supercomputing, under project nn9676k).

Appendix A. Supplementary data

Supplementary data to this article can be found online at https://doi.org/10.1016/j.oceaneng.2021.109130.

References

Berberović, E., van Hinsberg, N.P., Jakirlić, S., Roisman, I.V., Tropea, C., 2009. Drop impact onto a liquid layer of finite thickness: dynamics of the cavity evolution. Phys. Rev. 79 (3), 036306.
Borg, M., Utrera Ortigado, E., Collu, M., Brennan, F.P., 2013. Passive Damping Systems for Floating Vertical axis Wind Turbines Analysis. European wind energy Conference, pp. 3–7.
Bozonnet, P., Emery, A., 2015. CFD simulations for the design of offshore floating wind platforms encompassing heave plates. In: The Twenty-Fifth International Ocean and Polar Engineering Conference. International Society of Offshore and Polar Engineers.
Brown, S.A., Magar, V., Greaves, D.M., Conley, D.C., 2014. An evaluation of RANS turbulence closure models for spilling breakers. Coast. Eng. Proc. (34) 5-5.
Bruinsma, N., Paulsen, B., Jacobsen, N., 2018. Validation and application of a fully nonlinear numerical wave tank for simulating floating offshore wind turbines. Ocean Eng. 147, 647–658.
Burmester, S., Gueydon, S., Vaz, G., el Moctar, B., 2017. Surge decay simulations of a semi-submersible floating offshore wind turbine. In: Proceedings of the 20th Numerical Towing Tank Symposium, pp. 2–3.
Burmester, S., Vaz, G., el Moctar, O., 2020a. Towards credible CFD simulations for floating offshore wind turbines. Ocean Eng. 209, 107237.
Burmester, S., Vaz, G., Gueydon, S., el Moctar, O., 2020b. Investigation of a semi-submersible floating wind turbine in surge decay using CFD. Ship Technol. Res. 67 (1), 2–14.
Chakrabarti, S.K., 1994. Advanced series on ocean engineering. In: Offshore Structure Modeling, vol. 9. World scientific.
Chua, K.H., Clelland, D., Huang, S., Sworn, A., 2005. Model experiments of hydrodynamic forces on heave plates. Int. Conf. Offshore Mech. Arctic Eng. 943–948.
Cordle, A., Jonkman, J., 2011. State of the Art in Floating Wind Turbine Design Tools. National Renewable Energy Lab.(NREL), Golden, CO (United States).
Cozijn, H., Uittenbogaard, R., Brake, E.t., 2005. Heave, roll and pitch damping of a deepwater CALM buoy with a skirt. In: The Fifteenth International Offshore and Polar Engineering Conference. International Society of Offshore and Polar Engineers.
Devolder, B., Rauwoens, P., Troch, P., 2017. Application of a buoyancy-modified k-ω SST turbulence model to simulate wave run-up around a monopile subjected to regular waves using OpenFOAM®. Coast. Eng. 125, 81–94.
Dudley Brian, S., 1961. A single formula for the "law of the wall. J. Appl. Mech. 28 (3), 455–458.
Dunbar, A.J., Craven, B.A., Paterson, E.G., 2015. Development and validation of a tightly coupled CFD/6-DOF solver for simulating floating offshore wind turbine platforms. Ocean Eng. 110, 98–105.
Dütsch, H., Durst, F., Becker, S., Lienhart, H., 1998. Low-Reynolds-number flow around an oscillating circular cylinder at low Keulegan–Carpenter numbers. J. Fluid Mech. 360, 249–271.
Fan, W., Anglart, H., 2020. varRhoTurbVOF: a new set of volume of fluid solvers for turbulent isothermal multiphase flows in OpenFOAM. Comput. Phys. Commun. 247, 106876.
Ferziger, J.H., Perić, M., Street, R.L., 2002. Computational Methods for Fluid Dynamics. Springer.
Gao, Z., Efthymiou, M., Cheng, L., Zhou, T., Minguez, M., Zhao, W., 2020. Hydrodynamic damping of a circular cylinder at low KC: experiments and an associated model. Mar. Struct. 72, 102777.
Hirt, C.W., Nichols, B.D., 1981. Volume of fluid (VOF) method for the dynamics of free boundaries. J. Comput. Phys. 39 (1), 201–225.
Jacobsen, N.G., Fuhrman, D.R., Fredsøe, J., 2012. A wave generation toolbox for the open-source CFD library: OpenFOAM®. Int. J. Numer. Methods Fluid. 70 (9), 1073–1088.
Launder, B.E., Spalding, D.B., 1983. The Numerical Computation of Turbulent Flows, Numerical Prediction of Flow, Heat Transfer, Turbulence and Combustion. Elsevier, pp. 96–116.
Lefebvre, S., Collu, M., 2012. Preliminary design of a floating support structure for a 5 MW offshore wind turbine. Ocean Eng. 40, 15–26.
Lopez-Pavon, C., Souto-Iglesias, A., 2015. Hydrodynamic coefficients and pressure loads on heave plates for semi-submersible floating offshore wind turbines: a comparative analysis using large scale models. Renew. Energy 81, 864–881.
Menter, F., Ferreira, J.C., Esch, T., Konno, B., Germany, A., 2003a. The SST turbulence model with improved wall treatment for heat transfer predictions in gas turbines. Proc. Int. Gas Turbine Congr. 2–7.
Menter, F.R., Kuntz, M., Langtry, R., 2003b. Ten years of industrial experience with the SST turbulence model. Turbulence, Heat Mmass Transfer 4 (1), 625–632.
Moreno, J., Cameron, M., Thiagarajan, K.P., Mendoza, C.A.G., 2015. Hydrodynamic performance of heave plates on floating offshore wind turbine platforms. In: The Twenty-Fifth International Ocean and Polar Engineering Conference. International Society of Offshore and Polar Engineers.
Nallayarasu, S., Bairathi, K., 2014. Hydrodynamic response of spar hulls with heave damping plate using simplified approach. Ships Offshore Struct. 9 (4), 418–432.
Peiffer, A., Roddier, D., Aubault, A., 2011. Design of a point absorber inside the WindFloat structure. Int. Conf. Offshore Mech. Arctic Eng. 247–255.
Philip, N.T., Nallayarasu, S., Bhattacharyya, S., 2019. Experimental investigation and CFD simulation of heave damping effects due to circular plates attached to spar hull. Ships Offshore Struct. 14 (4), 396–411.
Rahman, M.M., Karim, M.M., Alim, M.A., 2007. Numerical investigation of unsteady flow past a circular cylinder using 2-D finite volume method. J. Nav. Architect. Mar. Eng. 4 (1), 27–42.
Robertson, A., Bachynski, E.E., Gueydon, S., Wendt, F., Schünemann, P., 2020a. Total experimental uncertainty in hydrodynamic testing of a semisubmersible wind turbine, considering numerical propagation of systematic uncertainty. Ocean Eng. 195, 106605.
Robertson, A., Gueydon, S., Bachynski, E., Wang, L., Jonkman, J., Alarcón, D., Amet, E., Beardsell, A., Bonnet, P., Boudet, B., 2020b. OC6 Phase I: Investigating the Underprediction of Low-Frequency Hydrodynamic Loads and Responses of a Floating Wind Turbine. TORQUE.
Robertson, A., Jonkman, J., Masciola, M., Song, H., Goupee, A., Coulling, A., Luan, C., 2014. Definition of the Semisubmersible Floating System for Phase II of OC4. No. NREL/TP-5000-60601. National Renewable Energy Lab.(NREL), Golden, CO (United States).
Robertson, A., Jonkman, J., Wendt, F., Goupee, A., Dagher, H., 2016. Definition of the OC5 DeepCwind Semisubmersible Floating System. Technical report NREL.
Robertson, A.N., 2017. Uncertainty Analysis of OC5-DeepCwind Floating Semisubmersible Offshore Wind Test Campaign. NREL/CP-5000-68035. National Renewable Energy Lab.(NREL), Golden, CO (United States).
Robertson, A.N., Wendt, F., Jonkman, J.M., Popko, W., Dagher, H., Gueydon, S., Qvist, J., Vittori, F., Azcona, J., Uzunoglu, E., 2017. OC5 project phase II: validation of global loads of the DeepCwind floating semisubmersible wind turbine. Energy Procedia 137, 38–57.
Sauder, T., Chabaud, V., Thys, M., Bachynski, E.E., Sæther, L.O., 2016. Real-time hybrid model testing of a braceless semi-submersible wind turbine: Part I—the hybrid approach. In: ASME 2016 35th International Conference on Ocean, Offshore and Arctic Engineering. American Society of Mechanical Engineers Digital Collection.
Tao, L., Dray, D., 2008. Hydrodynamic performance of solid and porous heave plates. Ocean Eng. 35 (10), 1006–1014.
Veritas, D.N., 2010. WADAM User Manual. Høvik, Norway.
Wang, B., Xu, Z., Li, C., Wang, D., Ding, Q., 2020. Hydrodynamic characteristics of forced oscillation of heave plate with fractal characteristics based on floating wind turbine platform. Ocean Eng. 212, 107621.
Wei, Y.-f., Yang, J.-m., Chen, X., 2010. A Review of the Hydrodynamic Performance of Heave Damping Plates on Spar Platform [J]. China Offshore Platform 6.
Weller, H.G., Tabor, G., Jasak, H., Fureby, C., 1998. A tensorial approach to computational continuum mechanics using object-oriented techniques. Comput. Phys. 12 (6), 620–631.
Wilcox, D.C., 1998. Turbulence Modeling for CFD. DCW industries La Canada, CA.
Zhang, S., Ishihara, T., 2018. Numerical study of hydrodynamic coefficients of multiple heave plates by large eddy simulations with volume of fluid method. Ocean Eng. 163, 583–598.